Resonant high-order harmonic generation driven by quantum light

Zhi-Hong Jiao(焦志宏)[1,†], Qian-Qian Li(李倩倩)[1], Jin-Xu Du(杜进旭)[1], Guo-Li Wang(王国利)[1], and Song-Feng Zhao(赵松峰)[1]

[1] *College of Physics and Electronic Engineering, Northwest Normal University, Key Laboratory of Atomic and Molecular Physics and Functional Materials of Gansu Province, Lanzhou 730070, People's Republic of China*

(Received xxx; accepted manuscript online xxx)

We theoretically demonstrate ultra-wideband resonant high-order harmonic generation (HHG) driven by quantum light. The resonant HHG spectra generated by the bright squeezed vacuum (BSV) state exhibit nearly twice the bandwidth compared to typical non-resonant HHG driven by BSV, enabling the cutoff to approach approximately 400 eV. The underlying mechanism of this significant broadening is analyzed by examining the yield of fluctuation amplitude-dependent coherent harmonics. We find that this broadening results from the weak sensitivity of the coherent harmonic yield to the fluctuation amplitude of BSV. Furthermore, by analyzing the dependence of the cutoff energy of resonant HHG on the BSV intensity and wavelength, we propose a revised formula for estimating the cutoff energy of BSV-driven resonant HHG.

Keywords: high-order harmonic generation, resonant potential, bright squeezed vacuum state, cutoff energy

PACS: 42.65.Ky, 42.50.Ct, 42.50.Ar
DOI: 10.1088/1674-1056/xxxxxx **CSTR:** 32038.14.CPB.xxxxxx

1. Introduction

High-order harmonic generation (HHG) is an extreme nonlinear process involving the interaction of ultra-short, intense laser pulses with matter. It has found a broad range of applications, including high-resolution imaging [1], ultrafast spectroscopy [2], and attosecond science [3–7]. Coherent-light-driven HHG from gases [8–13], liquids [14], and solids [15] has significantly advanced over the past several decades. In recent years, quantized-light-driven HHG has gradually attracted attention due to developments in experimental quantum optics that have effectively improved the efficiency of generating thermal and squeezed states. For instance, the bright squeezed vacuum (BSV) state has been employed for second-, third-, and fourth-harmonic generation [16]. Thermal light generated by superluminescent diodes or optical amplifiers has been shown to enhance two-photon fluorescence [17] and second-harmonic generation [18], respectively. Notably, ultra-short BSV pulses with output powers approaching 350 MW have been experimentally demonstrated [19,20], along with the regulation and control of their optical properties [21–23].

The quantized light driver provides an additional degree of freedom in the atomic HHG process, enabling effects such as extending the harmonic spectrum [24], modifying electronic trajectories [25,26], and generating attosecond pulses

*Project supported by the National Natural Science Foundation of China (Grant Nos. 12465025, 12364040, 12574315, and 12504322).
†Corresponding author. Email: jiaozh@nwnu.edu.cn
©2026 Chinese Physical Society and IOP Publishing Ltd

[27]. HHG emitted from solids driven by BSV light has been demonstrated experimentally [28,29]. To date, research on quantized-light-driven HHG has rapidly advanced in both theory and experiment. Although the foundational theory is well established, further theoretical investigation is required to fully understand unconventional HHG processes involving specialized targets or drivers. For instance, the influence of atomic structure, such as excited atomic states, on quantized-light-driven HHG remains unclear.

In this paper, we theoretically investigate BSV-driven HHG from a resonant-potential atomic system featuring a metastable state. An additional transition between the metastable and ground states induces resonance at a specific harmonic order. Our simulations demonstrate that the HHG spectra of the resonant-potential atom driven by BSV exhibit an exceptionally broad bandwidth. The cutoff energy of BSV-driven HHG from the resonant-potential atom is more than twice that of a Coulomb-potential atom under identical driving intensities. We explain this significant extension by analyzing the yield contribution of coherent harmonic components, corresponding to the fluctuation amplitudes of BSV, to the total spectrum. Additionally, we examine the influence of BSV intensity and wavelength on the cutoff energy. Since the conventional analytical cutoff formula is invalid for estimating the cutoff energy of the resonant HHG spectrum, we propose a revised formula by identifying the dependence of harmonic yield on driving intensity and wavelength.

2. Theoretical method

The joint density matrix $\boldsymbol{\rho}(t)$ of interaction between the intense quantized electromagnetic field and the atom satisfies the time-dependent Schrödinger equation [30]:

$$i\hbar\frac{\partial\boldsymbol{\rho}(t)}{\partial t}=\left[\widehat{H}_0,\boldsymbol{\rho}(t)\right], \tag{1}$$

where the Hamiltonian is composed of the atomic Hamiltonian, the electromagnetic-field Hamiltonian, and their interaction term: $\widehat{H}_0=\widehat{H}_A+\widehat{H}_F+\widehat{\boldsymbol{d}}\cdot\widehat{\boldsymbol{E}}(t)$. The term $\widehat{H}_A$ refers to the field-free bound electron, $\widehat{H}_F$ is the Hamiltonian of the electromagnetic field, and $\widehat{\boldsymbol{d}}\cdot\widehat{\boldsymbol{E}}(t)$ is the electric-dipole interaction between the electron and the quantized electromagnetic field. $\widehat{\boldsymbol{E}}(t)$ denotes the quantized electric-field operator. Gorlach *et al.* proposed [24] a method for solving the joint density matrix for a single-mode light field by employing the generalized Glauber P representation. According to this method, considering the limit of a small single-photon field amplitude, the density matrix can be written in the form

$$\begin{aligned}\boldsymbol{\rho}(t)=&\int \mathrm{d}^2\alpha\, Q(\alpha)\,|\phi_\alpha(t)\rangle\langle\phi_\alpha(t)|\\&\otimes\prod_{\substack{(\vec{k}_1\sigma_1),(\vec{k}_2\sigma_2)\\\neq(\vec{k}_0\sigma_0)}}|\gamma^\alpha_{\vec{k}_1\sigma_1}\rangle\langle\gamma^\alpha_{\vec{k}_2\sigma_2}|,\end{aligned} \tag{2}$$

where $Q(\alpha)$ is the Husimi function of the P representation, and $\phi_\alpha(t)$ is the electron wavefunction driven by a coherent state light field whose amplitude is denoted by the complex variable α. The squeezed state $\gamma^\alpha_{\vec{k}_1\sigma_1}$, whose mode is denoted by $\vec{k}_1\sigma_1$, is related to the induced dipole $\boldsymbol{d}_\alpha$:

$$\gamma^\alpha_{\vec{k}_1\sigma_1}=\frac{i}{\hbar}\epsilon^{(1)}\boldsymbol{d}_\alpha(\omega)\cdot\vec{e}_\sigma, \tag{3}$$

where $\epsilon^{(1)}$ refers to the so-called single-photon amplitude, which is determined by the volume of quantization V: $\epsilon^{(1)}=\sqrt{\hbar\omega/2\varepsilon_0 V}$. The semi-classical dipole induced by a coherent-state field is

$$\boldsymbol{d}_\alpha(\omega)=\int e^{i\omega t}\left\langle\phi_\alpha(t)\left|\widehat{\boldsymbol{d}}\right|\phi_\alpha(t)\right\rangle dt. \tag{4}$$

Taking the diagonal components of the electron state matrix, the density matrix of the emis-

sion field is

$$\boldsymbol{\rho}_{\rm F}(t) = {\rm Tr}_{\rm A}\big[\boldsymbol{\rho}(t)\big] = \int {\rm d}^2\alpha\, Q(\alpha)\, \|\phi_\alpha(t)\|^2 \times \prod_{\substack{(\vec{k}_1\sigma_1),\,(\vec{k}_2\sigma_2)\\ \neq(\vec{k}_0\sigma_0)}} |\gamma^\alpha_{\vec{k}_1\sigma_1}\rangle\langle\gamma^\alpha_{\vec{k}_2\sigma_2}|. \tag{5}$$

Here $\|\phi_\alpha(t)\|^2 = \langle\phi_\alpha(t)|\phi_\alpha(t)\rangle$. For the normalized TDSE solution, $\|\phi_\alpha(t)\|^2 = 1$. The total energy of the emission field is written as

$$\begin{aligned} E_{\rm emit} &= \sum_{\vec{k}\sigma} {\rm Tr}\big[\boldsymbol{\rho}_{\rm F}(t_{\rm off}) a^\dagger_{\vec{k}\sigma} a_{\vec{k}\sigma}\big] \\ &= \sum_{\vec{k}\sigma} \int {\rm d}^2\alpha\, Q(\alpha)\, \|\phi_\alpha(t_{\rm off})\|^2 |\gamma^\alpha_{\vec{k}\sigma}|^2, \end{aligned} \tag{6}$$

where the creation and annihilation operators $a^\dagger_{\vec{k}\sigma}$ and $a_{\vec{k}\sigma}$ only act on the squeezed states $\gamma^\alpha_{\vec{k}_1\sigma_1}$ and $\gamma^\alpha_{\vec{k}_2\sigma_2}$. Therefore, the frequency-dependent energy density of the emission field is simplified as

$$\frac{dE_{\rm emit}}{d\omega} = \frac{\omega^4}{6\pi^2\varepsilon_0 c^3} \int d^2\alpha\, Q(\alpha)\, |\boldsymbol{d}_\alpha(\omega)|^2, \tag{7}$$

where ε_0 and c denote the vacuum permittivity and the light speed. The dimensionless coherent state α is related to the classical electric-field amplitude by the single-photon field amplitude: $E_\alpha = 2\epsilon^{(1)}\alpha$. The Husimi function of the squeezed vacuum state is given by

$$Q(\alpha) = \frac{1}{8\pi\big(\epsilon^{(1)}\big)^2|\overline{\alpha}|^2} \exp\left(-\frac{|\alpha|^2}{2|\overline{\alpha}|^2}\right). \tag{8}$$

The semi-classical dipole $\boldsymbol{d}_\alpha(\omega)$ is calculated by numerically solving a one-dimensional time-dependent Schrödinger equation (1D-TDSE) in the presence of a classical laser field. In atomic units (a.u.), the 1D-TDSE is written in the form [31]

$$i\frac{\partial}{\partial t}\psi(x,t) = \left[-\frac{1}{2}\nabla^2 + V_0(x) + xE(t)\right]\psi(x,t). \tag{9}$$

Here, a one-dimensional resonant potential involving a metastable state is employed. It is a hydrogen-like model for describing ionic HHG involving the transition from the bound state to the autoionizing state. And it can well reproduce the resonant HHG spectrum using a low-dimensional calculation when the accurate contribution weights of time-domain trajectories are not required. A significant difference from the conventional Coulomb potential is that this potential possesses a double-shoulder structure [32], as shown in Fig. 1(a). This potential is written as

$$\begin{aligned} V_0(x) = &-\varepsilon + \frac{\varepsilon}{1+e^{(\beta+x)/\gamma}} \\ &+ \frac{\varepsilon}{1+e^{(\beta-x)/\gamma}} + \frac{\delta}{(x^2+\eta)\big(1+e^{(x+\beta)/\gamma}\big)} \\ &+ \frac{\delta}{(x^2+\eta)\big(1+e^{(\beta-x)/\gamma}\big)}. \end{aligned} \tag{10}$$

The relevant parameters are set as follows: $\varepsilon = 1.5$, $\beta = 1.27$, $\gamma = 0.23$, $\delta = 14$, and $\eta = 1.4$. Then the ground-state and the metastable-state eigenvalues are -15.78 eV and 32.65 eV, respectively. In the simulations, the B-spline basis expansion method and the split-operator technique are employed for solving the initial state and time-dependent wavefunctions, respectively. To ensure numerical convergence, the reasonable temporal grids 32768 over a duration of 9 o.c. and spatial grids 4096 on x=-400 $\sim$ 400 a.u. are set. And the absorbing boundary is at $x = 380$ a.u.

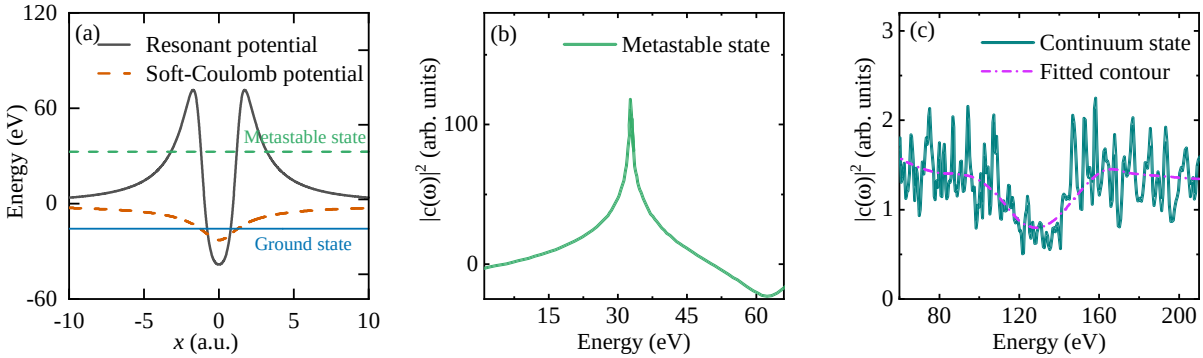


Fig. 1. The model potential (a); The metastable-state (b) [33] and continuum-state (c) probability of the resonant-potential atom as a function of energy.

This potential barrier can lead to the existence of harmonic resonance associated with the metastable state - ground state and the continuum state - ground state transitions. As pointed out by Tudorovskaya *et al.* [32], the metastable-state probability (the modulus squared of the metastable-state coefficient) obtained via the projection technique shows the position of the resonance, i.e., $\hbar\omega = 32.65 + 15.78 \approx 48$ eV, as shown in Fig. 1(b). In addition, this potential barrier leads to a minimum in the HHG spectrum, which is presented by the continuum-state probability, as shown in Fig. 1(c). This minimum located at 130 eV corresponds to the spectral minimum of the photon energy $\hbar\omega = 130+15.78 \approx 146$ eV. The continuum-state probability is extracted from the total wavefunction with the assistance of a mask function [33,34]:

$$c\left(\frac{p^2}{2}\right) = \int dt \int dx\ \psi(x,t)M(x)e^{-ixp}, \qquad (11)$$

where the mask function is

$$M(x) = \begin{cases} 0, & |x| \le x_b, \\ 1 - \exp\left[-\sigma(|x| - x_b)\right], & \text{else.} \end{cases} \qquad (12)$$

3. Results and discussion

3.1. Spectral characteristics of resonant HHG driven by BSV

First, we present the spectral characteristics of the BSV-driven resonant HHG by numerically solving Eq. (7). In the calculations, the intensity of BSV light with a wavelength of $\lambda_0 = 800$ nm is set as $I_{\rm vac} = \frac{1}{2}\varepsilon_0 c|E_{\rm vac}|^2 = 10^{14}$ W/cm^2. This intensity magnitude has been achieved through advancements in photonic-crystal fiber technology; for example, a femtosecond BSV pulse with an intensity of 3.5×10^{14} W/cm^2 (pulse energy approximately 350 nJ for a beam spot diameter of ~ 10 μm) was demonstrated in a relevant experiment [20]. Meanwhile, the short pulse duration is chosen considering a short lifetime of the metastable state of the target atom, which is approximately 1.3 optical cycles (o. c.) for an energy-level width of ~ 0.0071 a.u. The driving envelope is expressed in the form of

$$f(t) = \begin{cases} \sin^2\left(\frac{\pi t}{2t_{\rm on}}\right) & \text{rising edge}, \\ 1 & \text{plateau}, \\ \sin^2\left(\frac{\pi(t-t_{\rm p})}{2t_{\rm off}}\right) & \text{falling edge}. \end{cases} \qquad (13)$$

Here the pulse plateau that is slightly longer than the lifetime is set as 2 o. c., and the rising and falling edges are both 3.5 o. c.

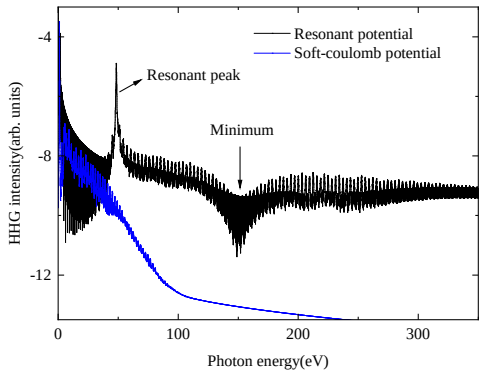


Fig. 2. The BSV-driven HHG spectra with the resonant potential (black line) and the soft-Coulomb potential (blue line). The resonant HHG exhibits a resonant peak near 48 eV and a minimum around 146 eV.

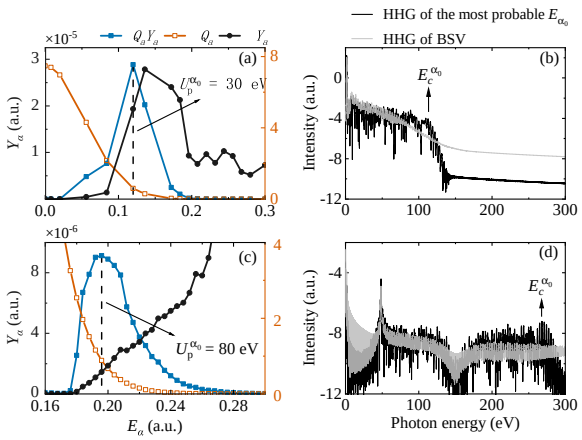


Fig. 3. Comparison of the HHG cutoff energies ($E_c^{\alpha 0} = I_p + 3.17U_p^{\alpha 0}$) with two types of potentials: the coherent-harmonic intensity Y_α (black solid circles), Husimi distribution Q_α (red hollow squares), and the product $Q_\alpha Y_\alpha$ (blue solid squares) as functions of the fluctuation amplitude E_α with the Coulomb potential (a) and the resonant potential (c); and the corresponding spectra with the Coulomb potential (b) and the resonant potential (d).

In Fig. 2, we present a comparison of the harmonic spectra generated from atoms modeled with resonant-potential and soft-Coulomb potentials, both driven by BSV light. For both types of atomic samples, identical driving intensities and the same ground-state eigenvalues were used to ensure a fair comparison. The spectra of the two samples exhibit significant differences. In addition to the distinctive features of the resonant peak (photon energy ~48 eV) and a minimum (photon energy ~146 eV), the HHG spectrum from the resonant-potential atom shows a pronounced broadening of the plateau compared to that of the soft-Coulomb potential atom. The cutoff energy of the former reaches approximately 280 eV, whereas that of the latter is around 100 eV. The spectral plateau of the latter can be predicted by an analytical formula [24]

$$E_{\text{cutoff}} = \frac{3.05 I_p}{(4\hbar)^{2/3}(2\pi c)^2} I_{\text{vac}}^{2/3} \lambda_0^2 + I_p. \tag{14}$$

According to Eq. (14), the estimated cutoff energy is $\sim$ 108 eV. However, obviously, this formula is invalid for predicting the spectral plateau of the resonant HHG.

To clarify the broadening difference between the two atomic samples, we extract the yield contribution of coherent harmonics corresponding to different fluctuation amplitudes. According to Eq. (7), for an arbitrary fluctuation amplitude of BSV, this contribution is determined by both the coherent-harmonic intensity Y_α and the Husimi distribution Q_α. In Fig. 3, these quantities and their product are shown as functions of E_α. For the Coulomb-potential atom, the integral intensity over 108–124 eV increases rapidly and then decreases with fluctuation amplitude. For the resonant-potential atom, the integral intensity over 232–465 eV grows much more slowly over a broader amplitude range. Consequently, the product $Q_\alpha Y_\alpha$ peaks at a larger effective amplitude for the resonant system. The most probable amplitudes determined from $Q_\alpha Y_\alpha$ correspond to ponderomotive energies of approximately 30 eV and 80 eV for the Coulomb and resonant potentials, respectively. The cutoff energies $I_p + 3.17U_p^{\alpha 0}$ of the coherent harmonics associated with these amplitudes agree with the cutoffs of the corresponding BSV-driven HHG spectra, as shown in Figs. 3(b) and 3(d). Thus, the cutoff of BSV-

driven resonant HHG can be determined from the most probable fluctuation amplitude.

3.2. Dependence of the HHG cutoff on the BSV intensity and wavelength

Next, we present the influence of BSV intensity and wavelength on the cutoff energy of the resonant harmonic spectrum. Fig. 4 compares three resonant-harmonic samples with different intensities. The coherent-harmonic intensity Y_α has a similar amplitude E_α dependence for all three samples, whereas the Husimi distribution broadens with increasing BSV intensity. Consequently, the most probable amplitude increases with BSV intensity and the resonant harmonic spectrum broadens continuously, as shown in Fig. 4(d).

Fig. 5 compares three harmonic samples at wavelengths of 800, 1000, and 1200 nm. Although the most probable fluctuation amplitude decreases as the wavelength increases, the ponderomotive energy, which depends on both amplitude and wavelength, increases. The cutoff energy of the coherent HHG driven by the most probable amplitude therefore increases with wavelength, and the corresponding BSV-driven harmonic spectrum broadens continuously, as illustrated in Fig. 5(d).

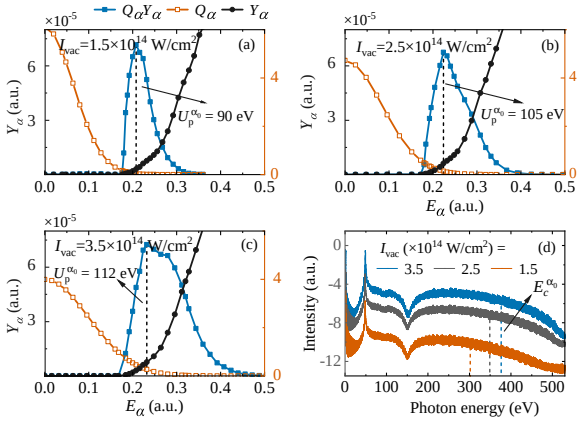


Fig. 4. Influence of the BSV intensity on the cutoff energy of resonant HHG: Y_α (black solid circles), Q_α (red hollow squares), and $Q_\alpha Y_\alpha$ (blue solid squares) as functions of fluctuation amplitude at different intensities in (a)-(c), and the corresponding spectra in (d).

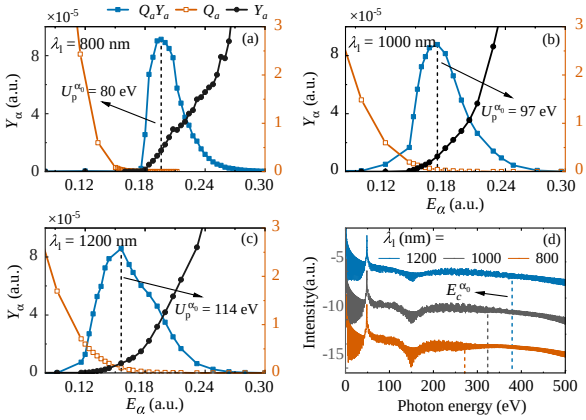


Fig. 5. Influence of the BSV wavelength on the cutoff energy of resonant HHG: Y_α, Q_α, and $Q_\alpha Y_\alpha$ as functions of fluctuation amplitude for different wavelengths in (a)-(c), and the corresponding spectra in (d).

3.3. Empirical formula of the cutoff energy of the BSV-driven resonant HHG

Finally, to effectively estimate the cutoff energy of the BSV-driven resonant HHG, we revise Eq. (14) proposed by Gorlach *et al.*. Through numerical calculation, the cutoff energy as a function of the BSV intensity and wavelength is shown in Fig. 6. The corresponding empirical fitting formula can be expressed as

$$E_{\text{cutoff}} = aI_{\text{vac}}^{\sigma}\left(\text{W/cm}^2\right)\lambda_{\text{l}}^{\vartheta}(\text{nm}) + b, \qquad (15)$$

where the four fitted coefficients are $a = 47.26$, $b = 0$, $\sigma = 0.3$, and $\vartheta = 0.8$, respectively. Obviously, these coefficients differ from those in Eq. (14) because Eqs. (14) and (15) are derived using two different methods. In the approach proposed by Gorlach et al. [24], the derivation of Eq. (14) is based on the assumption of complete recombination probability; that is, the coherent-harmonic intensity can be replaced by the ionization probability when all continuum-state electrons recombine to the ground state. In this approach, the ionization probability is approximated using the ADK model [35]. Both of these substitutions may intro-

duce unavoidable errors in estimating the coherent-harmonic intensity, especially for HHG from the resonant-potential atom. For example, in the BSV-driven resonant HHG shown in Fig. 2, because the resonant-potential barrier with a double shoulder structure is wider than the Coulomb-potential barrier, the ionization probability for the resonant-potential atom could be significantly overestimated by the ADK model, which is typically accurate only for the Coulomb potential. Consequently, the cut-off energy estimated by Eq. (14) is much smaller than the value obtained from numerical calculations for the BSV-driven resonant HHG.

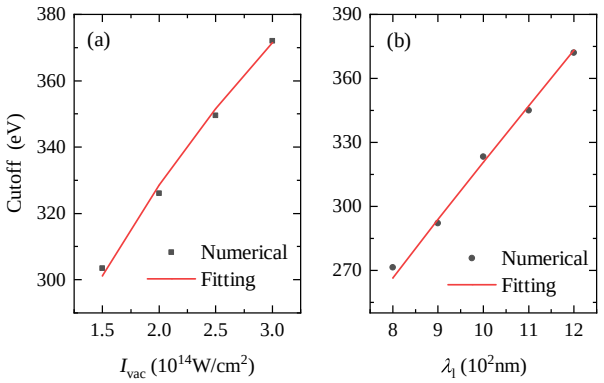


Fig. 6. The cut-off energy as a function of the BSV intensity (a) and wavelength (b).

4. Conclusion

It is theoretically demonstrated that the BSV-driven high-order harmonic generation (HHG) spectrum can be significantly broadened by employing a resonant potential. The spectrum of resonant HHG exhibits nearly twice the bandwidth compared to conventional HHG from atoms with a Coulomb potential. To elucidate the mechanism behind this substantial broadening, we analyze the yield contributions of coherent harmonics corresponding to different fluctuation amplitudes of BSV within the total spectrum. The yield increases more slowly with fluctuation amplitude in the case of the resonant-potential atom than in the usual Coulomb-potential atom, leading to this broadening effect. To effectively predict the cutoff energy of BSV-driven resonant HHG, we present the dependence of resonant HHG on BSV intensity and wavelength, and propose an empirical formula based on fitting the numerical results.

References

[1] Kfir O, Zayko S, Nolte C, Sivis M, Möller M, Hebler B, Arekapudi S S P K, Steil D, Schäfer S, Albrecht M, Cohen O, Mathias S and Ropers C 2017 *Sci. Adv.* **3** eaao4641

[2] Heinrich T, Taucer M, Kfir O, Corkum P B, Staudte A, Ropers C and Sivis M 2021 *Nat. Commun.* **12** 3723

[3] Paul P M, Toma E S, Breger P, Mullot G, Augé F, Balcou P, Muller H G and Agostini P 2001 *Science* **292** 1689

[4] Krausz F and Ivanov M 2009 *Rev. Mod. Phys.* **81** 163

[5] Villeneuve D M 2018 *Contemp. Phys.* **59** 47

[6] Wang X W, Xiao F, Wang J C, Wang L, Zhang B, Liu J L, Zhao J and Zhao Z X 2024 *Ultrafast Sci.* **4** 80

[7] Shirozhan M, Mondal S, Grósz T *et al.* 2024 *Ultrafast Sci.* **4** 0067

[8] McPherson A, Gibson G, Jara H, Johann U, Luk T S, McIntyre I A, Boyer K and Rhodes C K 1987 *JOSA B* **4** 595

[9] Ferray M, L'Huillier A, Li X F, Lompré L A, Mainfray G and Manus C 1988 *J. Phys. B: At. Mol. Opt. Phys.* **21** L31

[10] Krause J L, Schafer K J and Kulander K C 1992 *Phys. Rev. Lett.* **68** 3535

[11] Hu J, Wang Y C, Jing Q S, Jiang W, Wang G W, Zhao Y W, Xiao B, Liang H J and Ma R 2024 *Chin. Phys. B* **33** 054208

[12] Zhou S S, Li Y L, Zhao Z X, Xing M, Xu N, Wang H, Wang J, Zhao X and Hu M H 2025 *Chin. Phys. B* **34** 063202

[13] Wang Y, Li Y L, Qiao Y, Gao N, Guo F M, Chen Z, He L H, Yang Y J, Zhao X and Wang J 2024 *Chin. Phys. B* **33** 034212

[14] Luu T T, Yin Z, Jain A, Gaumnitz T, Pertot Y, Ma J and Wörner H J 2018 *Nat. Commun.* **9** 3723

[15] Ghimire S, DiChiara A D, Sistrunk E, Agostini P, DiMauro L F and Reis D A 2011 *Nat. Phys.* **7** 138

[16] Manceau M, Spasibko K Y, Leuchs G, Filip R and Chekhova M V 2019 *Phys. Rev. Lett.* **123** 123606

[17] Jechow A, Seefeldt M, Kurzke H, Heuer A and Menzel R 2013 *Nat. Photonics* **7** 973

[18] Qu Y and Singh S 1992 *Opt. Commun.* **90** 111

[19] Iskhakov T S, Pérez A M, Spasibko K Y, Chekhova M V and Leuchs G 2012 *Opt. Lett.* **37** 1919

[20] Finger M A, Iskhakov T S, Joly N Y, Chekhova M V and Russell P S J 2015 *Phys. Rev. Lett.* **115** 143602

[21] Agafonov I N, Chekhova M V and Leuchs G 2010 *Phys. Rev. A* **82** 011801

[22] Pérez A M, Iskhakov T S, Sharapova P, Lemieux S, Tikhonova O V, Chekhova M V and Leuchs G 2014 *Opt. Lett.* **39** 2403

[23] Sharapova P R, Frascella G, Riabinin M, Pérez A M, Tikhonova O V, Lemieux S, Boyd R W, Leuchs G and Chekhova M V 2020 *Phys. Rev. Res.* **2** 013371

[24] Gorlach A, Tzur M E, Birk M, Krüger M, Rivera N, Cohen O and Kaminer I 2023 *Nat. Phys.* **19** 1689

[25] Tzur M E, Birk M, Gorlach A, Krüger M, Kaminer I and Cohen O 2023 *Nat. Photonics* **17** 501

[26] Rivera-Dean J, Stammer P, Ciappina M F and Lewenstein M 2025 *Phys. Rev. Lett.* **135** 013801

[27] Wang S J, Lai X Y and Liu X J 2025 *Phys. Rev. A* **112** L011102

[28] Rasputnyi A, Chen Z, Birk M, Cohen O, Kaminer I, Krüger M, Seletskiy D, Chekhova M and Tani F 2024 *Nat. Phys.* **20** 1960

[29] Lemieux S, Jalil S A, Purschke D N, Boroumand N, Hammond T J, Villeneuve D, Naumov A, Brabec T and Vampa G 2025 *Nat. Photonics* **19** 767

[30] Landau L D and Lifshitz E M 1977 *Quantum mechanics: Non-Relativistic Theory*, 3rd edn. (Oxford: Pergamon Press) pp. 38–40

[31] Kulander K C 1988 *Phys. Rev. A* **38** 778

[32] Tudorovskaya M and Lein M 2011 *Phys. Rev. A* **84** 013430

[33] Tong X M, Hino K and Toshima N 2006 *Phys. Rev. A* **74** 031405

[34] Ma M Y, Wang J P, Jing W Q, Guan Z, Jiao Z H, Wang G L, Chen J H and Zhao S F 2021 *Opt. Express* **29** 33245

[35] Ammosov M V, Delone N B and Krainov V P 1986 *Sov. Phys. JETP* **64** 1191